Viser Technology Pte. Ltd.
Research and Application of Materials Science
DOI: 10.33142/rams.v4i2.8468

Research Article Open Access

Effects of Nickel on the Microstructure, Mechanical properties and Corrosion Resistance of $CoCrFeNi_xAl_{0.15}Ti_{0.1}$ High Entropy Alloy

Wu QI [1, 3], Yitian SU [1, 3], Xiao YANG [2*], Guannan ZHANG [2], Yi ZHAO[4], Ya ZHANG[5], Wenrui WANG[1, 3*]

1 School of Mechanical Engineering, University of Science and Technology Beijing, Beijing 100083, China
2 Key Laboratory of Cryogenics, Technical Institute of Physics and Chemistry, Chinese Academy of Sciences, Beijing 100190, China
3 Key Laboratory of Fluid Interaction with Material, Ministry of Education, Beijing 100083, China
4 Unit 92228, People's Liberation Army, Beijing 100072, PR China
5 Beijing Aerospace Petrochemical Technology & Equipment Engineering Corporation Limited, Beijing 100176, China

***Corresponding Author:** Xiao YANG, E-mail: yangxiao@mail.ipc.ac.cn; Wenrui WANG, E-mail: gmbitwrw@ustb.edu.cn*

Abstract:
The present work investigates the effect of Ni on the microstructure, mechanical properties, and corrosion resistance of $CoCrFeNi_xAl_{0.15}Ti_{0.1}$ high-entropy alloys. It was found that the appropriate addition of Ni element in the alloy is beneficial to reduce the average grain size of the alloy. The yield strength and tensile strength of the alloy under fine-grain strengthening have also been increased, while the ductility of the system in this study has not been significantly affected. In terms of corrosion resistance, $CoCrFeNi_xAl_{0.15}Ti_{0.1}$ high-entropy alloys form a dense passive film at open circuit potential, possessing good corrosion resistance. However, with the excessive addition of Ni content in the alloy, the pitting corrosion resistance of the alloy in the environment of chloride ions will decrease due to the relative decrease of the relative content of Cr element. This work also can provide guidances for the design and development of new precipitation-strengthened CoCrFeNi-based high-entropy alloys with excellent comprehensive properties.

***Keywords:** High-entropy alloy, Microstructures, Mechanical properties, Corrosion resistance*

1 Introduction

In recent years, high-entropy alloys (HEAs) have become a hot research object in the field of metal materials for its excellent comprehensive properties [1-5]. Different from the design concept of traditional alloys with a single principal element, HEAs containing four or more elements designed in equal or near-equal proportions tend to form a multi-component disordered solid solution phase structure [6-7]. Due to excellent ductility at room temperature and low temperature, the most representative CoCrFeNi high-entropy alloy with FCC structure has been widely studied [8-9]. Additionally, the CoCrFeNi alloys can form a uniform, dense and stable high-entropy amorphous oxide passive film on the surface in an oxygen environment, which can lead to excellent corrosion resistance [10-12]. However, the low strength of FCC-structured CoCrFeNi high-entropy alloys limits the range of industrial applications.

In the past few years, many researches have been carried out on strengthening CoCrFeNi HEAs. In traditional structural alloys, such as superalloys, steels, aluminum alloys, etc., precipitation strengthening has been proven to be one of the effective ways to improve the strength of metal materials [13-15]. Due to the multi-component characteristics of CoCrFeNi-based HEA, there are many types of strengthening phases can be induced to precipitate. Common precipitation strengthening phases include Laves phase and L12-γ′ phase [16-18]. However, though the addition of common Nb, Hf, Ta and other large-sized atoms to form the precipitation of Laves phase can improve the mechanical properties of the alloy, it will also seriously reduce the toughness of the alloys [19-21]. A large number of studies have confirmed that L_{12} phase precipitation strengthening is one of the effective methods to achieve the strength-ductility balance of CoCrFeNi-based HEAs. Yang et al. added a fixed stoichiometric ratio of Ni and Al to the CoCrFeNi HEAs to form a nano-L12 precipitate on the FCC matrix, which effectively improved the strength and maintained good plasticity [22]. He et al. induced the formation of L_{12} coherent nano-γ′ phase in CoCrFeNi HEA by adding a small amount of Al

Received on November 2, 2022; Accepted on December 8, 2022

and Ti, successfully achieving the balance of strength-ductility [23].

For CoCrFeNi HEAs, the corrosion resistance of the alloy can be effectively improved by adding certain alloying elements, which has become one of the important directions of research on the corrosion resistance of HEAs [24-26]. Studies have shown that the composition of the precipitated phase of the alloys and the degree of element segregation directly affect the overall corrosion resistance of the HEA. For example, in the AlxCoCrFeNi alloy, the increasing of the Al content will lead to an increase in the volume fraction of the Cr-depleted body-centered cubic phase, which will reduce the local corrosion resistance [27]. Nevertheless, with the homogenization heat treatment, the degree of element segregation between the precipitated phase and the matrix is reduced, resulting in improving the corrosion resistance of the alloys [28]. Therefore, the composition and compositional regulation of the phase structure play a key role in the corrosion resistance of the alloy. Similar to iron and steel materials, Ni element usually plays the role of austenite stabilization, that is, the higher the content of Ni element, the more stable the FCC structure multi-component solid solution in the HEA. Meanwhile, other phases in the alloys (e.g., BCC structural solid solution phase and B2 phase, σ phase, Laves phase, and other ordered phases) are also gradually suppressed with increasing Ni content [29-30]. In the CoCrFeNi-TiAl HEAs system, the addition of Ti and Al elements will enhance the mechanical properties by forming ordered γ′ strengthening phases, but also consume the group elements in the matrix during the formation of γ′ phases. In particular, the reduction of Ni element in the matrix will lead to a decrease in the stability of the FCC structure matrix, which may lead to a decrease in the corrosion resistance of the matrix, and in turn greatly affect the overall corrosion resistance.

Thus, the main emphasis of this study is to designs and prepares the $CoCrFeNi_xAl_{0.3}Ti_{0.2}$ (x=1.0, 1.25, 1.5, 1.75) HEAs, and to explores the effect of Ni content on the structure, mechanical properties and corrosion resistance of $CoCrFeNi_xAl_{0.15}Ti_{0.1}$ HEAs, as well as to optimize the alloys performance. This work will help to extend the excellent overall performance CoCrFeNi-based HEAs system to provide an important research basis.

2 Material and methods

The $CoCrFeNi_xAl_{0.3}Ti_{0.2}$ HEAs ingots were prepared by melting in vacuum melting furnace using Co, Cr, Fe, Ni, Al, Ti with high-purity (＞ 99.9 wt.%) as raw materials under argon protection. During the smelting process, the samples were re-melted five times at least to ensure the uniformity of the elements. The alloy samples were homogenized at 1200℃ for 18 hours, subsequently by water quenching. All homogenized samples were cold-rolled with a thickness reduction of 60 %, and then aged at 800℃ for 4 h.

The crystal structures of the $CoCrFeNi_xAl_{0.3}Ti_{0.2}$ alloys were examined by X-ray diffractometer (Model D8/Advance, Bruker, Germany) using Cu-Kα radiation with a scanning range of 30 to 90 ° and a step size of 5 °/min. The fracture surfaces of the tensile samples were studied using a scanning electron microscopy (SEM, HITACHI S-4300, Japan). Mechanical tensile tests were performed the dog-bone shaped tensile specimens with 20 × 4 × 2 mm at room temperature by a universal testing machine (CMT4305, New Sansi Laboratory Equipment Co., China) under a strain rate of 5×10^{-4}/s. Electrochemical measurements were carried out using an electrochemical workstation (VersaStat4, Princeton, USA), with a three-electrode system in 3.5 wt.% NaCl solution at room temperature. In three-electrode system, the HEA specimen, platinum electrode and saturated calomel electrode (SCE) were employed as the working, auxiliary and reference electrode, respectively. Before the electrochemical test, all samples were immersed at least 30 minutes until the open circuit potential (OCP) reached a steady state. The potentiodynamic-polarization tests were measured from from an initial potential of -0.25 V (vs. OCP) to the anodic potential with a current density of 2 mA/cm^2 with a scan speed of 1 mV/s. The electrochemical impedance spectroscopy (EIS) was measured at the OCP in the frequency range of 10^5 Hz to 10^{-2} Hz with a potential amplitude of 10 mV.

3 Results

3.1 Microstructure and phase analysis

The XRD patterns of $CoCrFeNi_xAl_{0.15}Ti_{0.1}$ (x=1, 1.25, 1.5, 1.75) HEAs are shown in Figure1. It can be seen that the obvious FCC solid solution structure peaks were identified in all alloys. In general, adding an appropriate amount of Al and Ti to CoCrFeNi alloys is beneficial to the formation of nanoscale L12-γ′ phase, which can be confirmed in TEM experiments in previous work [31].

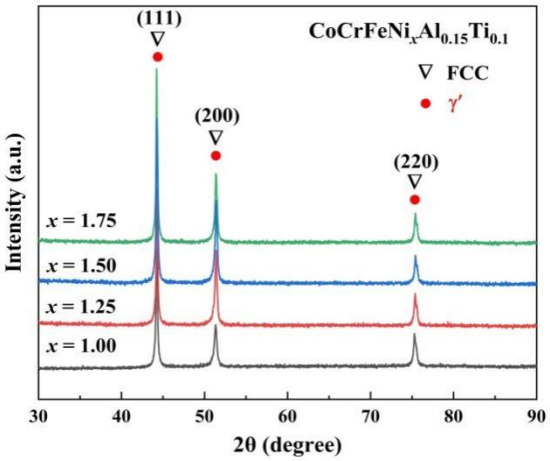

Figure 1 XRD pattern of $CoCrFeNi_xAl_{0.15}Ti_{0.1}$ HEAs

To explore the effect of Ni element content on the phase transition temperature range of HEAs, DSC tests were carried out on $CoCrFeNi_xAl_{0.15}Ti_{0.1}$ alloys with different Ni contents, and the results are shown in Figure 2. As can be seen, with the increase of the Ni content, the

melting point of the HEAs decreases gradually. It should be pointed out that the DSC curves of the four components of the alloys have an obvious exothermic step in the temperature rise stage, indicating that there is an obvious precipitate phase dissolves into the solid-matrix of $CoCrFeNi_xAl_{0.15}Ti_{0.1}$ HEAs during heat treatment temperature. When the Ni content increases from x=1 to x=1.75, the precipitation temperature of ordered γ′ phase in the alloys decreases slowly from 904℃ to 898℃, showing that the addition of Ni element will reduce the thermal stability of the precipitated phase.

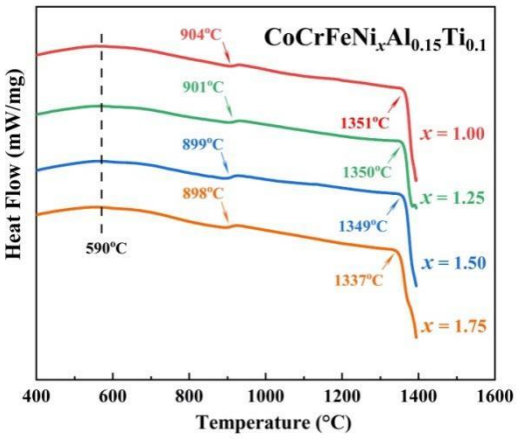

Figure 2 DSC spectrum of $CoCrFeNi_xAl_{0.15}Ti_{0.1}$ (x=1, 1.25, 1.5, 1.75) HEAs

Figure 3 shows the EBSD invert pole figure (IPF) and grain size distribution of $CoCrFeNi_xAl_{0.15}Ti_{0.1}$ HEAs. The HEA grains of the four alloys are basically in an equiaxed state, while the orientation distribution is uniform. Moreover, the grains have no obvious preferred orientation distribution, and there are no large deformed grains. With the increase of Ni content, the average grain size of the alloys decreases first and then increases. The average grain size of $CoCrFeNi_xAl_{0.15}Ti_{0.1}$ HEAs decreased from 14.4μm to 7.6μm when Ni content increased from x=1 to x=1.25. But as the Ni content continues to increase, the average grain size of the x=1.75 alloy begins to increase to 10.7μm. Previous research has shown that the grain size has a direct effect on the strength of the metal, that is, fine grain strengthening [32]. With the gradual refinement of the grains, the number of grain boundaries inside the alloy increases rapidly, resulting in an increase in the hindrance of the grain boundaries to the movement of dislocations during the deformation process, which improves the mechanical properties of the HEAs. Figure4 displays the kernel average misorientation (KAM) maps of $CoCrFeNi_xAl_{0.15}Ti_{0.1}$ HEAs samples. The KAM values generally can be represented as the density of geometrically necessary dislocation (GND) [33]. It can be seen that the dislocations in all alloys are distributed near the grain boundaries. Under the same rolling deformation and heat treatment conditions, the dislocation density in Figure 4(a, c and d) is lower. However, the KAM value in the x=1.25 alloy is significantly higher, indicating that the dislocation density of the alloy accumulated at the grain boundary is greater, which is conducive to improving the initial strain hardening rate of the alloy under small plastic deformation [34].

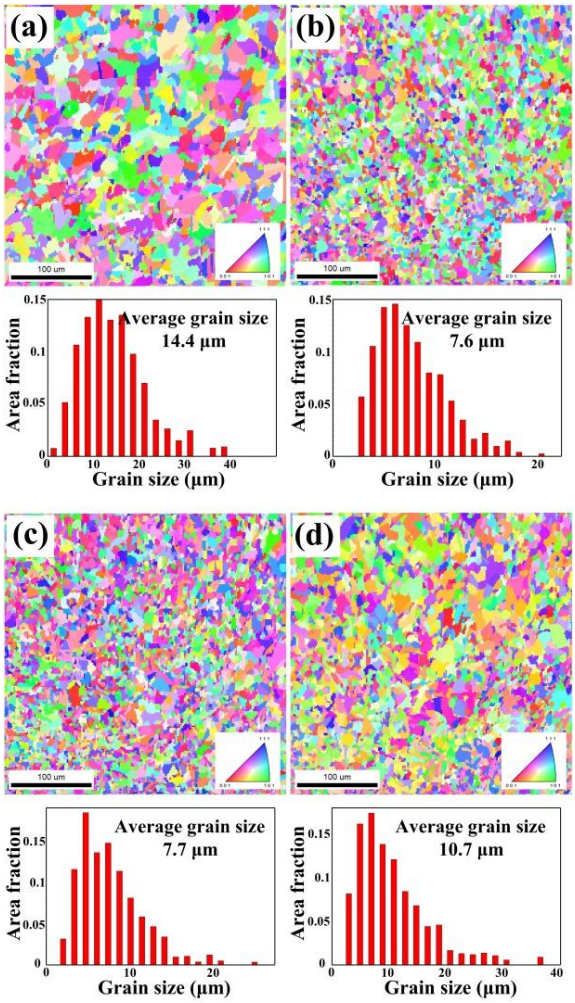

Figure 3 The IPF and grain size distribution of $CoCrFeNi_xAl_{0.15}Ti_{0.1}$ HEAs: (a) x=1, (b) x=1.25, (c) x=1.5, (d) x=1.75

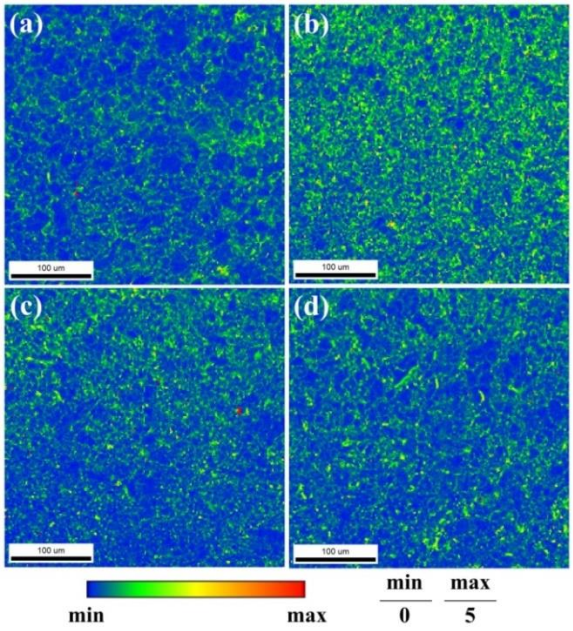

Figure 4 The KAM maps of $CoCrFeNi_xAl_{0.15}Ti_{0.1}$ HEAs: (a) x=1, (b) x=1.25, (c) x=1.5, (d) x=1.75

3.2 Mechanical properties

The tensile engineering stress-strain curves at room temperature of the $CoCrFeNi_xAl_{0.15}Ti_{0.1}$ HEAs are shown in Figure 5(a). Table.1 summarizes the yield strength (σ_{YS}), ultimate tensile strength (σ_{UTS}) and fracture elongation (ε_{FE}) of HEAs. The four components of $CoCrFeNi_xAl_{0.15}Ti_{0.1}$ HEAs exhibiting continuous work hardening behavior until the final plastic instability, while there is no discontinuous yield phenomenon in the transition stage between elastic deformation and plastic deformation. It can be found that as the Ni content increased to x=1.25, the comprehensive mechanical properties of the $CoCrFeNi_{1.25}Al_{0.15}Ti_{0.1}$ HEAs reached the optimum, and the yield strength, ultimate tensile strength and fracture elongation were 800.4 MPa, 1172 MPa and 27.1%, respectively. After the end of the elastic stage, $CoCrFeNi_{1.25}Al_{0.15}Ti_{0.1}$ HEAs exhibits a short yield plateau and begins to show significant work-hardening behavior after the end of the yield stage. As the Ni content continues to increase, the mechanical properties of the $CoCrFeNi_xAl_{0.15}Ti_{0.1}$ HEAs begin to decline, and the plastic deformation ability also decreases. Figure 5 (b) shows the work-hardening behavior of $CoCrFeNi_xAl_{0.15}Ti_{0.1}$ HEAs. All alloys exhibit a typical multi-stage work-hardening rate curve. The first stage is the transition from elastic to plastic deformation. Due to the low density of mobile dislocations at the onset of plastic deformation, the work hardening rate rapidly decreases to a negative value, which corresponds to the yield drop in the engineering stress-strain curve. The second stage of work hardening increases significantly, which may be related to the twinning related deformation mechanisms generated during deformation [4,35]. The anomalous increase in strain hardening rate in this stage is crucial for maintaining the plastic stability of the alloy [36]. The third stage of work-hardening rate decreases slowly and corresponds to the longer plastic deformation phase of the engineering stress-strain curve. In this stage, the work-hardening rate gradually decreases until a local stress concentration occurs, leading to catastrophic fracture.

Table 1 The yield strength, ultimate tensile strength and fracture elongation of $CoCrFeNi_xAl_{0.15}Ti_{0.1}$ HEAs

Alloys	σ_{YS} (MPa)	σ_{UTS} (MPa)	ε_{FE} (%)
$CoCrFeNiAl_{0.15}Ti_{0.1}$	739.8	1142.6	29.1
$CoCrFeNi_{1.25}Al_{0.15}Ti_{0.1}$	800.4	1172.9	27.1
$CoCrFeNi_{1.5}Al_{0.15}Ti_{0.1}$	778.9	1156.2	24.9
$CoCrFeNi_{1.75}Al_{0.15}Ti_{0.1}$	745.0	1121.3	24.5

Figure 6 is the SEM image of the tensile sample fracture of $CoCrFeNi_xAl_{0.15}Ti_{0.1}$ HEAs. A large number of dimples and a small number of cleavage fracture planes can be found in the tensile sections of all samples, meaning that the tensile fracture modes of the four groups of samples are dominated by ductile fracture and shear fracture. In general, the size of fracture dimples is related to the size of grains, because grain boundaries are the starting point of pores. The finer the grain, the smaller the dimple size [37]. In addition, the separation of the precipitated phase and the matrix during deformation and the fragmentation of the precipitated phase can also lead to the formation of pores [38]. Thus, the dimples at the fracture of the samples with Ni content of x=1.25 and x=1.5 are smaller, while the number of cleavage fracture planes is also increase. This may be related to the promotion of the precipitation of γ' phase after a small increase in Ni content. On the one hand, the formation of precipitated phases causes the strengthening effect of the second phase. On the other hand, the precipitated phases can also play a role in refining grains [39]. When the Ni content continued to increase to x=1.75, the dimple depth at the fracture site of the sample began to become shallower, and the cleavage area began to increase, indicating a decrease in the ductile fracture of the sample.

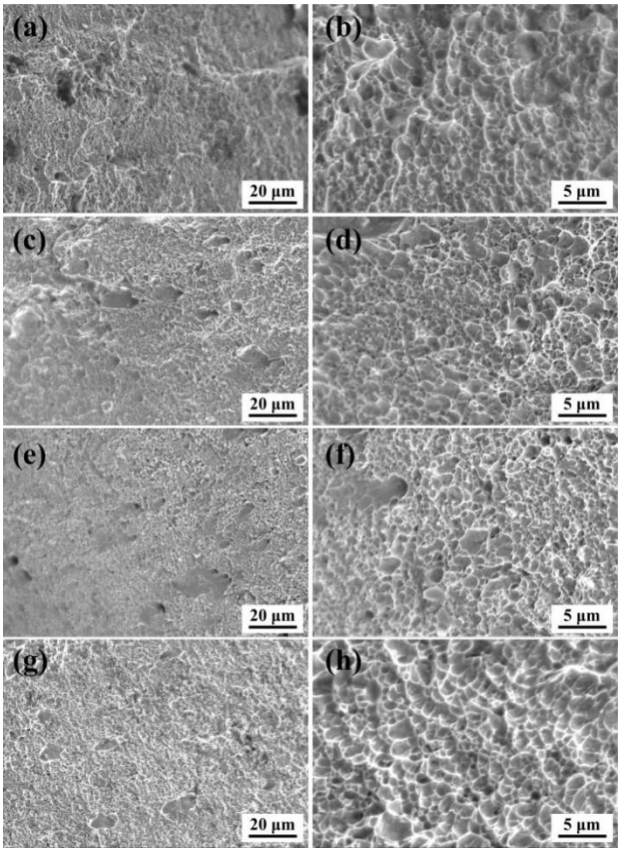

Figure 6 Fracture morphology and high-magnification fracture morphology of tensile samples of $CoCrFeNi_xAl_{0.15}Ti_{0.1}$ HEA: (a, b) x=1, (c, d) x=1.25, (e, f) x=1.5, (g, h) x=1.75

3.3 Corrosion resistance

Figure 7 illustrates the potential polarization curves of the $CoCrFeNi_xAl_{0.15}Ti_{0.1}$ HEAs under 3.5 wt.% NaCl solution at room temperature. The results of the electrochemical corrosion parameters (corrosion potential Ecorr, corrosion current icorr) are listed in Table 2. It can be found that the polarization curves of $CoCrFeNi_xAl_{0.15}Ti_{0.1}$ HEAs are similar, showing the same active-to-passive corrosion behavior. Based on electrochemical theory, the lower the corrosion current of a material, the better its corrosion resistance. Thus, all

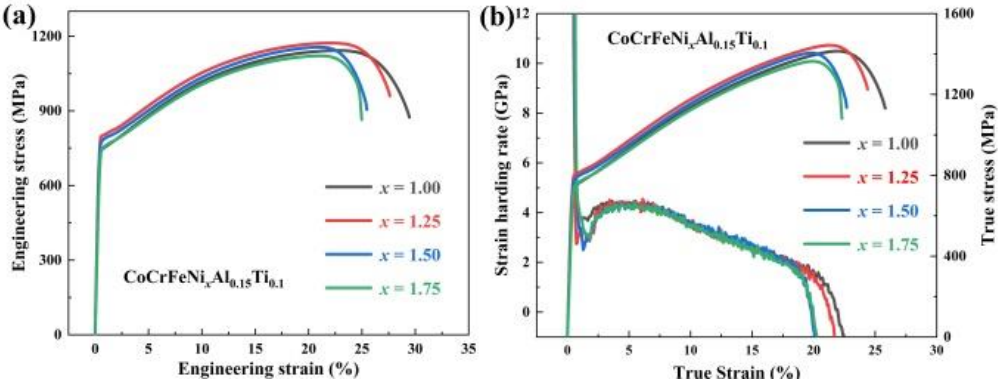

Figure 5 The mechanical properties of $CoCrFeNi_xAl_{0.15}Ti_{0.1}$ (x=1, 1.25, 1.5, 1.75) HEAs at room temperature (a) engineering stress-strain, (b) true stress-strain curve and work hardening rate

$CoCrFeNiAl_{0.15}Ti_{0.1}$ HEAs demonstrate better corrosion resistance. Additionally, the dislocations also play a great influence on the corrosion resistance of alloys, which will promote the passive film on the surface of the alloys and the diffusion of cation vacancies within the matrix [40]. These point defects in the environment of chlorine-containing corrosive solutions will accelerate the destruction of the surface passive film, reducing the corrosion resistance of the alloys. With the increase of Ni element in the alloys to x=1.25, the corrosion current density of the alloys reaches 9.19×10^{-8}A/cm^2, indicating that the corrosion resistance of x=1.25 alloy are the worst at the corrosion potential. However, the corrosion current density of the all alloys still maintains the same order of magnitude, implying that the HEA of this system possess good corrosion resistance.

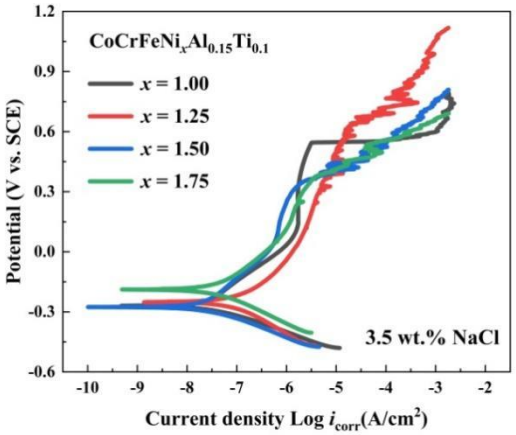

Figure 7 Potentiodynamic polarization curves of $CoCrFeNi_xAl_{0.15}Ti_{0.1}$ HEAs

In the corrosion resistance of materials, the pitting potential (Epit) is an important performance index parameter that characterizes the material's pitting resistance. Although the corrosion current density of $CoCrFeNi_{1.25}Al_{0.15}Ti_{0.1}$ HEAs is the highest, the breakdown potential reaches 0.639 V (vs. SCE), indicating that the formation of passive film of this component is more stable at high potentials. With the further increase of Ni element, the pitting corrosion potential of the material gradually decreases. Previous studies have shown that Cr element is a key element of stainless steel. In seawater, Cr element can form a dense Cr_2O_3 film on the surface of stainless steel, which greatly improves the resistance of the material to the erosion of chloride ions [41]. For $CoCrFeNi_xAl_{0.15}Ti_{0.1}$ HEAs, when the content of Ni in the alloy is excessive, the reduction of pitting corrosion resistance in the alloys may be related to the reduction of the relative content of Cr in the alloys.

Table 2 Corrosion kinetic parameters of $CoCrFeNi_xAl_{0.15}Ti_{0.1}$ HEAs

Alloys	Ecorr (V_{SCE})	Icorr (A/cm^2)	Epit (V_{SCE})
$CoCrFeNiAl_{0.15}Ti_{0.1}$	-0.265	2.86×10^{-8}	0.544
$CoCrFeNi_{1.25}Al_{0.15}Ti_{0.1}$	-0.256	9.19×10^{-8}	0.639
$CoCrFeNi_{1.5}Al_{0.15}Ti_{0.1}$	-0.268	3.23×10^{-8}	0.356
$CoCrFeNi_{1.75}Al_{0.15}Ti_{0.1}$	-0.187	3.89×10^{-8}	0.379

In order to further understand the corrosion mechanism of $CoCrFeNi_{1.25}Al_{0.15}Ti_{0.1}$ HEAs under the open circuit potential, the material was analyzed by EIS test. Figure 8 shows the Nyquist plot and Bode plot results of $CoCrFeNixAl_{0.15}Ti_{0.1}$ HEAs. All response results present a single capacitive semicircle, indicating a passive film with the same structure. For the Nyquist plot, the larger the diameter of the arc, the more stable the passive film formed on the surface of the alloys [42]. In Figure 8 (a), the corrosion resistance trend of $CoCrFeNi_xAl_{0.15}Ti_{0.1}$ HEAs is basically consistent with the potentiodynamic polarization curve. In addition, Figure 8 (b) shows the Bode plots of different alloys, and the phase angles of all alloys tend to be -80 ° in a wide frequency range, meaning a stable passive film is formed on the surface of the alloys.

According to the semicircular arc characteristics of the Nyquist plot and the corrosion characteristics of the alloys, Figure 8 (a) shows the equivalent circuit applicable to the alloy system. In this circuit, Rs and Rt represent the resistance of the solution and the passive film, respectively [43]. Based on this fitting circuit simulation, the electrochemical impedance fitting parameters of the $CoCrFeNi_xAl_{0.15}Ti_{0.1}$ HEAs are listed in Table.3. Generally, the higher the resistance Rt of the passive film, the better the protective effect of the passive film. Thus, $CoCrFeNiAl_{0.15}Ti_{0.1}$ HEAs display

better passive film stability at open circuit potential.

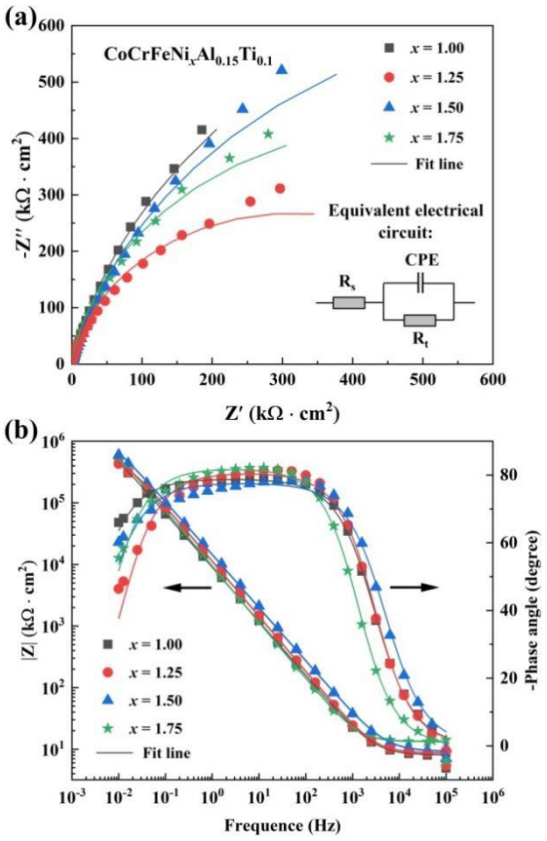

Figure 8 EIS response of $CoCrFeNi_xAl_{0.15}Ti_{0.1}$ HEAs: (a) Nyquist plot and equivalent circuit, (b) Bode plot

Table 3 Impedance fitting parameters of $CoCrFeNixAl_{0.15}Ti_{0.1}$ by the equivalent circuit.

Alloys	Rs /Ω*cm^2	Y (CPE) /(F*cm^{-2})	n	Rt /Ω*cm^2
$CoCrFeNiAl_{0.15}Ti_{0.1}$	7.99	2.23×10^{-5}	0.88	1.73×10^{6}
$CoCrFeNi_{1.25}Al_{0.15}Ti_{0.1}$	8.60	1.70×10^{-5}	0.90	6.30×10^{5}
$CoCrFeNi_{1.5}Al_{0.15}Ti_{0.1}$	9.18	1.41×10^{-5}	0.86	1.53×10^{6}
$CoCrFeNi_{1.75}Al_{0.15}Ti_{0.1}$	13.26	2.00×10^{-5}	0.91	9.70×10^{5}

4 Conclusions

In this work, the effects of Ni on the microstructure, mechanical properties and corrosion resistance of $CoCrFeNi_xAl_{0.15}Ti_{0.1}$ HEAs have been systematically investigated, and the main conclusions are as follows:

$CoCrFeNi_xAl_{0.15}Ti_{0.1}$ HEAs consists of a typical dual-phase structure of FCC + γ′ phases. The crystals in the all alloys exhibit equiaxed crystal morphology, and the $CoCrFeNi_{1.25}Al_{0.15}Ti_{0.1}$ alloy has the smallest grain size, with an average grain size of 7.6 μm.

The yield strength and tensile strength of $CoCrFeNi_xAl_{0.15}Ti_{0.1}$ HEAs increased first and then decreased with the increase of Ni content, but the tensile plasticity remained at a high level. Especially, the yield strength and tensile strength of $CoCrFeNi_{1.25}Al_{0.15}Ti_{0.1}$ alloy reached 800 MPa and 27.1%, respectively.

Due to the formation of a stable passive film on the surface, $CoCrFeNi_xAl_{0.15}Ti_{0.1}$ HEAs display good corrosion resistance under corrosion potential. Excessive Ni element in the alloy will reduce the pitting corrosion resistance of the alloy.

Acknowledgements

This work is supported by the National Key R&D Program of China (Grant No. 2020YFA0405700), the Inner Mongolia Science and Technology Major Project (No. 2020ZD0011).

References

[1] E.P. George, D. Raabe, R.O. Ritchie, High-entropy alloys, Nature Reviews Materials [J].2029, 4(8): 515-534.

[2] Q. Ding, Y. Zhang, X. Chen, et al.. Tuning element distribution, structure and properties by composition in high-entropy alloys, Nature [J].2019, 574(7777): 223-227.

[3] C.M. Lin, H.L. Tsai, H.Y. Bor. Effect of aging treatment on microstructure and properties of high-entropy Cu0.5CoCrFeNi alloy, Intermetallics [J].2010,18(6): 1244-1250.

[4] G. Laplanche, A. Kostka, O.M. Horst, et al.. Microstructure evolution and critical stress for twinning in the CrMnFeCoNi high-entropy alloy, Acta Mater [J]. 2016(118): 152-163.

[5] X. Yang, Y. Zhang. Prediction of high-entropy stabilized solid-solution in multi-component alloys, Mater. Chem. Phys. 2012,132(2): 233-238.

[6] Z.G. Wang, W. Zhou, L.M. Fu, et al.. Effect of coherent L12 nanoprecipitates on the tensile behavior of a fcc-based high-entropy alloy, Mater. Sci. Eng. 2017(696): 503-510.

[7] W. Wang, W. Qi, L. Xie, X. Yang, J. Li, Y. Zhang, Microstructure and Corrosion Behavior of (CoCrFeNi)95Nb5 High-Entropy Alloy Coating Fabricated by Plasma Spraying, Materials. 2019,12(5): 694.

[8] W. Qi, W. Wang, X. Yang, et al.. Effect of Zr on phase separation, mechanical and corrosion behavior of heterogeneous CoCrFeNiZrx high-entropy alloy, J Mater Sci Technol. 2022(109): 76-85.

[9] W. Huo, F. Fang, H. Zhou, et al.. Remarkable strength of CoCrFeNi high-entropy alloy wires at cryogenic and elevated temperatures, Scripta Mater. 2017(141): 125-128.

[10] P. Wu, K. Gan, D. Yan, et al.. A non-equiatomic FeNiCoCr high-entropy alloy with excellent anti-corrosion performance and strength-ductility synergy, Corros. Sci. 2021(183): 13.

[11] H. C. Liu, C. W. Tsai. Effect of Ge addition on the microstructure, mechanical properties, and corrosion behavior of CoCrFeNi high-entropy alloys, Intermetallics. 2021(132):47.

[12] Y. Fu, J. Li, H. Luo, et al.. Recent advances on environmental corrosion behavior and mechanism of high-entropy alloys, J Mater Sci Technol. 2021(80): 217-233.

[13] E. Nembach, G. Neite. Precipitation hardening of superalloys by ordered γ′-particles, Prog. Mater Sci. 1985,29(3): 177-319.

[14] W. F. Miao, D. E. Laughlin. Precipitation hardening in aluminum alloy 6022, Scripta Mater. 1999,40(7): 873-878.

[15] M. J. Yao, E. Welsch, D. Ponge, et al.. Strengthening and strain hardening mechanisms in a precipitation-hardened high-Mn lightweight steel, Acta Mater. 2017(140):258-273.
[16] D. Chen, F. He, B. Han, et al.. Synergistic effect of Ti and Al on L12-phase design in CoCrFeNi-based high entropy alloys, Intermetallics. 2019(110):67-68.
[17] W.H. Liu, T. Yang, C.T. Liu. Precipitation hardening in CoCrFeNi-based high entropy alloys, Mater. Chem. Phys. 2018(210):2-11.
[18] Y. Yu, F. He, Z. Qiao, et al.. Effects of temperature and microstructure on the triblogical properties of CoCrFeNiNbx eutectic high entropy alloys, J. Alloys Compd. 2019(775): 1376-1385.
[19] W. Liu, J. He, H. Huang, et al.. Effects of Nb additions on the microstructure and mechanical property of CoCrFeNi high-entropy alloys, Intermetallics. 2015(60): 1-8.
[20] H. Ma, C.H. Shek, Effects of Hf on the microstructure and mechanical properties of CoCrFeNi high entropy alloy, J. Alloys Compd. 2020(827):456.
[21] H. Jiang, K. Han, D. Qiao, et al.. Effects of Ta addition on the microstructures and mechanical properties of CoCrFeNi high entropy alloy, Mater. Chem. Phys. 2018(210): 43-48.
[22] F. Zheng, G. Zhang, X. Chen, et al.. A new strategy of tailoring strength and ductility of CoCrFeNi based high-entropy alloy, Mater. Sci. Eng. 2020(774):98-102.
[23] J.Y. He, H. Wang, H.L. Huang, et al.. A precipitation-hardened high-entropy alloy with outstanding tensile properties, Acta Mater. 2016(102): 187-196.
[24] W. Wang, J. Wang, Z. Sun, et al.. Effect of Mo and aging temperature on corrosion behavior of (CoCrFeNi)100-xMox high-entropy alloys, J. Alloys Compd. 2020(812):152139.
[25] Y. J. Hsu, W. C. Chiang, J. K. Wu, Corrosion behavior of FeCoNiCrCux high-entropy alloys in 3.5% sodium chloride solution, Mater. Chem. Phys. 2005,92(1): 112-117.
[26] P. Muangtong, A. Rodchanarowan, D. Chaysuwan, et al.. The corrosion behaviour of CoCrFeNi-x (x=Cu, Al, Sn) high entropy alloy systems in chloride solution, Corros. Sci. 2020(172):1-2.
[27] Y. Shi, B. Yang, X. Xie, et al.. Corrosion of AlxCoCrFeNi high-entropy alloys: Al-content and potential scan-rate dependent pitting behavior, Corros. Sci. 2017(119): 33-45.
[28] Y. Shi, L. Collins, R. Feng, et al.. Homogenization of AlxCoCrFeNi high-entropy alloys with improved corrosion resistance, Corros. Sci. 2018(133):120-131.
[29] C. Liu, W. Peng, C.S. Jiang, et al.. Composition and phase structure dependence of mechanical and magnetic properties for AlCoCuFeNix high entropy alloys, J Mater Sci Technol. 2019,35(6):1175-1183.
[30] C. C. Juan, C. Y. Hsu, C. W. Tsai, et al.. On microstructure and mechanical performance of AlCoCrFeMo0.5Nix high-entropy alloys, Intermetallics. 2013,32(0):401-407.
[31] W. Qi, W. Wang, X. Yang, et al.. Effects of Al and Ti co-doping on the strength-ductility- corrosion resistance of CoCrFeNi-AlTi high-entropy alloys, J. Alloys Compd. 2022(925):166751.
[32] S. Gangireddy, B. Gwalani, R.S. Mishra. Grain size dependence of strain rate sensitivity in a single phase FCC high entropy alloy Al0.3CoCrFeNi, Mater. Sci. Eng. 2018(736): 344-348.
[33] J. Su, D. Raabe, Z. Li. Hierarchical microstructure design to tune the mechanical behavior of an interstitial TRIP-TWIP high-entropy alloy, Acta Mater. 2019(163): 40-54.
[34] N.K. Adomako, G. Shin, N. Park, et al.. Laser dissimilar welding of CoCrFeMnNi-high entropy alloy and duplex stainless steel, J Mater Sci Technol. 2021(85): 95-105.
[35] W.H. Liu, Z.P. Lu, J.Y. He, et al.. Ductile CoCrFeNiMox high entropy alloys strengthened by hard intermetallic phases, Acta Mater. 2016(116): 332-342.
[36] T. Yang, Y.L. Zhao, J.H. Luan, et al.. Nanoparticles-strengthened high-entropy alloys for cryogenic applications showing an exceptional strength-ductility synergy, Scripta Mater. 2019(164):30-35.
[37] M. H. Cai, C. Y. Lee, Y. K. Lee. Effect of grain size on tensile properties of fine-grained metastable β titanium alloys fabricated by stress-induced martensite and its reverse transformations, Scripta Mater. 2012,66(8): 606-609.
[38] O. León-García, R. Petrov, L.A.I. Kestens. Void initiation at TiN precipitates in IF steels during tensile deformation, Mater. Sci. Eng. 2010,527(16-17): 4202-4209.
[39] J. He, N. Li, S.K. Makineni, et al.. Effects of minor Nb alloying on the thermal stability and mechanical responses of a γ/γ′ type high-entropy alloy with high Fe content, Mater. Sci. Eng. 2022(851):6-8.
[40] Y. Wang, J. Jin, M. Zhang, et al.. Influence of plastic deformation on the corrosion behavior of CrCoFeMnNi high entropy alloy, J. Alloys Compd. 2022(891):79-92.
[41] J. B. Lee. Effects of alloying elements, Cr, Mo and N on repassivation characteristics of stainless steels using the abrading electrode technique, Mater. Chem. Phys. 2006,99(3): 224-234.
[42] Z. Xu, H. Zhang, X. Du, et al.. Corrosion resistance enhancement of CoCrFeMnNi high-entropy alloy fabricated by additive manufacturing, Corros. Sci. 2020(177):34-36.
[43] H. Luo, Z. Li, A.M. Mingers, et al.. Corrosion behavior of an equiatomic CoCrFeMnNi high-entropy alloy compared with 304 stainless steel in sulfuric acid solution, Corros. Sci. 2018(134): 131-139.